JOURNAL OF PROPULSION AND POWER
Vol. 20, No. 3, May–June 2004

Numerical Simulation of Separated Cold Gas Nozzle Flows

A. Gross*
University of Arizona, Tucson, Arizona 85721
and
C. Weiland†
European Aeronautic Defence and Space Company, 81663 Munich, Germany

A numerical method for the simulation of separated cold gas nozzle flows is presented and applied to six subscale nozzles. The nozzles considered were a truncated ideal nozzle, two thrust-optimized parabolic nozzles, and three dual bell nozzles. For the thrust-optimized parabolic contours, the occurrence of free and restricted shock separation and the cap shock pattern are discussed. Comparisons with experimental data are provided. Shortcomings of the numerical method are pointed out.

Nomenclature

a, A_0, A_s	=	realizability constants
c	=	speed of sound
c_F	=	skin-friction coefficient
c_μ	=	turbulence model constant
e	=	total energy
$\boldsymbol{F}$	=	flux vector
J	=	cell volume
k	=	turbulence kinetic energy
M	=	Mach number
P_k	=	turbulence kinetic energy production term
Pr	=	Prandtl number
p	=	static pressure
$\boldsymbol{Q}$	=	state vector
Re	=	Reynolds number
r	=	radius
S	=	total strain
$\boldsymbol{S}$	=	source term vector
s	=	arc length
T	=	temperature
t	=	time
V	=	contravariant velocity
v	=	velocity
y	=	displacement
W	=	total vorticity
x	=	physical coordinate
α, β	=	turbulence model constants
γ	=	ratio of specific heats
κ	=	thermal conductivity
μ	=	viscosity
ξ	=	transformed coordinate
ρ	=	density
σ	=	turbulence model constant
ω	=	turbulence dissipation

Subscripts

a	=	ambient state
c	=	chamber
CL	=	centerline
i	=	incipient separation
i, j, k	=	direction
$,i$	=	derivative in i direction
T	=	turbulence
th	=	nozzle throat
w	=	wall

Superscript

v	=	viscous

Received 29 May 2003; revision received 16 October 2003; accepted for publication 17 October 2003.

*Postdoctoral Student, Aerospace and Mechanical Engineering Department, 1130 North Mountain Avenue; agross@email.arizona.edu.

†Manager, European Aeronautic Defence and Space Company; claus.weiland@space.eads.net. Member AIAA.

Introduction

NOZZLES used during a rocket's ascent through Earth's atmosphere experience a large fall off in ambient pressure. Their operational time in the rarefied higher atmosphere is usually longer than in the high-pressure lower atmosphere. These nozzles are, therefore, optimized for a low ambient pressure and overexpanded at ground level. As the nozzle area ratio and, thereby the overexpansion at ground level, are increased, the engine can produce higher vacuum impulse. However, the onset of flow separation limits the maximum possible area ratio.

During the moon program, considerable effort was put into the development of empirical separation prediction criteria.[1] It is desirable to avoid flow separation upstream of the nozzle exit because the unsteady nature of the uncontrolled separated flow causes undesirable aerodynamic forces on the nozzle wall. It also adversely affects the nozzles efficiency. Furthermore, the nozzle wall downstream of the separation would be exposed to high-thermal loads. This situation may be relieved by suction of ambient air that leads to convective cooling or by appropriate thermal protection design measures. During the startup of rocket engine motors, the flow separation region moves from the nozzle throat to the nozzle exit. During this phase, significant side loads may occur due to nonaxisymmetric flow separation. The same is true for the motor shutdown. The prevention of these aerodynamic side loads and vibrations is the motivation behind all efforts to avoid uncontrolled flow separation.

Two separation shock patterns are known in thrust-optimized parabolic nozzles. These separation patterns were named free shock separation (FSS) and restricted shock separation (RSS) by Nave and Coffey[2] (Figs. 1 and 2). The unique characteristic of thrust-optimized parabolic nozzles is a pronounced internal shock wave originating at the nozzle throat. The interaction of this internal shock wave with the normal shock may lead to RSS. One of the most prominent features of RSS, when compared with FSS, is a strong centerline reverse flow behind the separation shock (as indicated in Fig. 2). This reverse flow is induced by a vortex ring that encloses the axis. It may convect disturbances upstream and, thus, change the position of the normal shock in an unsteady fashion. The vortex ring also deflects the separated supersonic nozzle flow toward the wall

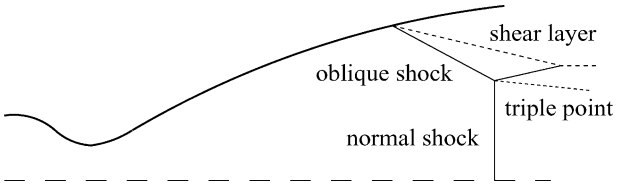

Fig. 1 Schematic of FSS.

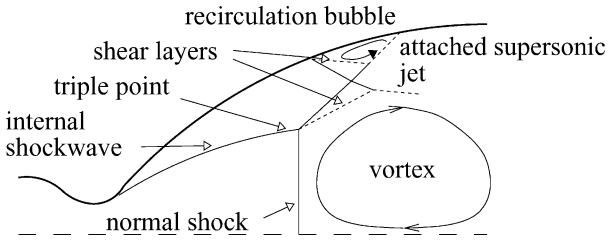

Fig. 2 Schematic of RSS.

and may cause it to reattach, thereby enclosing a small separation bubble. Based on a momentum balance, predictions can be made for this flow reattachment.[3]

For RSS, the static pressure in the separation bubble is always below ambient pressure. The flow separation point is, therefore, farther downstream for RSS than for FSS. The wall pressure in the reattachment region is considerably lower when in RSS than it would be if the flow were in FSS. If in FSS, the separation would be farther upstream and that region of the wall would be exposed to near ambient pressure. A flow hysteresis causes the switch from RSS to FSS during startup to occur at a higher pressure ratio (chamber pressure to ambient pressure), p_c/p_a, than the switch from FSS back to RSS during shutdown.

Another phenomenon associated with RSS is the opening of the separation bubble (as it reaches the nozzle exit during startup) and the aerodynamic forces associated with it. However, this purely two-dimensional thinking may be misleading. Photographs of the flow separation region taken in J-2, Vulcain, and the space shuttle main engine (SSME) show the separation line to have a zigzag appearance, which was named tepee-pattern by Nave and Coffey.[2] One may speculate that a three-dimensional flow instability mechanism or even a fluid structure interaction may cause this pattern. Although the side loads were not above average during the time when the tepee-pattern was observed, the occurrence of these distinctive structures serves as a reminder of the complexity of the real flow when compared with all numerical and model approaches. A sudden asymmetric switch from FSS to RSS and the subsequent opening of the recirculation bubble during startup are possibly two major contributors to side loads.[3–6] The same reasoning may be applied to the shutdown transient where the same phenomena occur in reversed order.

The flow in hot, full-scale nozzles can be interpreted as a complex interaction of several different physical phenomena. The exhaust gas is usually a mixture of hot combustion gases at high supersonic speeds. The flow is turbulent and unsteady and is subjected to different instability mechanisms, for example, shear layer or Görtler like instabilities. The separation shock vibrates at acoustic frequencies, and the entire nozzle structure undergoes vibration and deformation. A large number of other phenomena may be considered. The formulation of a theory that embraces all relevant aspects appears as challenging as the layout of an all-inclusive numerical method.

To gain insight into the flow physics, cold gas experiments were performed by various researchers. In these experiments, the number of unknowns was reduced. The gas composition and operating conditions were well known, the nozzle structure itself was very stiff, and data acquisition was easy because the sensors and cameras were not exposed to hot gases.

During the last years, different subscale cold gas nozzles were designed and tested by the Volvo Aero Corporation (VAC), the European Aeronautic Defence and Space Company (EADS-ST), and the German Aerospace Center (DLR). Six of the various nozzle contours used in these tests were chosen for the numerical simulations presented herein. A truncated ideal contour (TIC) by DLR (DLR TIC) was chosen as a reference case. Two thrust-optimized parabolic contours, one by DLR (DLR PAR) and one by VAC (VAC S1), were chosen because they clearly showed both RSS and FSS in the experiment and in previous numerical simulations.[7,30]

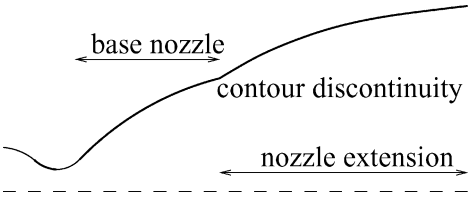

Fig. 3 Schematic of dual bell nozzle.

In an effort to gain a passive adaption of the nozzle area ratio to the decreasing ambient pressure during the rocket's ascent, several dual bell nozzle geometries (Fig. 3) were designed and tested by EADS-ST and others. The design goal was to have flow separation at the contour discontinuity (the interface of the base nozzle and the extension) at ground level conditions and to have the nozzle flow full in vacuum conditions. Therefore, the area ratio can be larger for vacuum operation resulting in a larger vacuum impulse.[8–10]

The Tehora nozzle, which was designed in a joint effort by EADS-ST and the Chemical Automatics Design Bureau (CADB)[8,10] and two dual bell nozzles by EADS-ST were investigated. The latter two, a truncated ideal base with constant wall pressure extension (TICCP) and a thrust-optimized parabolic base with constant wall pressure extension (PARCP), feature almost constant wall pressure in the second section of the nozzle. The idea was to have the separation point move rapidly (because the wall pressure gradient in the extension is zero) to the nozzle exit when the ambient pressure drops below a certain value. Interestingly, the pressure ratio where the separation line "jumps" from the contour discontinuity to the nozzle exit during startup is higher than the pressure ratio where the separation line moves back from the exit to the discontinuity during shutdown.[8]

The DLR TIC and PAR nozzles were tested at the P6 test facility at DLR in Germany.[11] At P6, the nozzles were operated in an altitude chamber where the optional use of a diffuser allows for a lowering of the test chamber pressure. Care had to be taken to avoid a coupling of nozzle and diffuser flow. The test gas was nitrogen. The VAC S1 was tested at the HYP500 testing facility at the Aeronautical Research Institute (FFA) in Sweden.[7] The test gas was compressed air, and the nozzle was operated in ambient atmosphere. The Tehora nozzle was tested at the Keldysh Research Center in Moscow[10] with both hot and cold air. The test data shown herein were obtained from the cold air tests. The two other dual bell contours were also tested at P6.[8]

Numerical simulations may aid the engineering community in the interpretation and analysis of nozzle test data. In numerical simulations, various stages of model complexity can be implemented. The flow can be treated as steady/unsteady, axisymmetric/three dimensional, chemically reacting/perfect gas, etc. Fluid–structure interaction can be taken into account, and turbulence models of different complexity can be employed. The different modules can be turned on/off to investigate separately the effect of the different phenomena. However, because of their immense complexity, the realistic simulation of full-scale hot gas nozzle flows still appears to be an insurmountable challenge. Although simulations may allow for additional insights into the flow physics, they can not, at the present development stage, be regarded as an alternative to full-scale nozzle testing within the framework of an engine development and qualification. To validate existing codes and existing models, the simulation of cold gas nozzle experiments appears to be the first logical step in the development of better numerical prediction tools.

Since the early 1980s, attempts have been made to simulate numerically separated nozzle flow. Chen et al.[12] presented numerical

simulations of a scaled down J-2 nozzle using the Baldwin–Lomax turbulence model. The simulations showed only FSS during startup; during shutdown, RSS was predicted for a certain intermediate pressure ratio range. This clearly indicated the possibility of an FSS/RSS hysteresis region for thrust-optimized parabolic nozzles. A somewhat coarsely resolved simulation of the Vulcain nozzle with a shock-fitting method was performed by Nasuti and Onofri.[13] This simulation also exhibited RSS, but the numerical method appeared to be less well suited for separated nozzle flow simulations. Experimental and numerical results for the VAC S1 subscale nozzle were given by Mattsson et al.[7] They associated the side load peaks observed in the experiments with certain features of the flowfield observed at the same pressure ratios in the numerical simulations (switch FSS↔RSS, opening of the recirculation bubble). Hunter presented results for another cold gas subscale nozzle.[14] He managed to achieve excellent flow separation location predictions with a two equation explicit algebraic stress model. However, the nozzle he chose did not feature RSS. Hence, the question remains unanswered, if a more elaborate turbulence model can improve the predictive quality for more complex separation shock patterns. Three-dimensional nozzle flow simulations by Schröder and Behr[15] with an asymmetric pressure gradient imposed at the inflow showed an only minor asymmetry of the separation line. The conclusion is that flow asymmetries at the nozzle inflow are not a likely explanation for side loads.

Numerical Method

Governing Equations

For the numerical simulations shown in this paper, the Favre-averaged Navier–Stokes equations in conservative form were solved in curvilinear coordinates ξ_i. In the following, repeated indices indicate summations (Einstein notation). The general formulation of the Navier–Stokes and turbulence transport equations is

$$J\frac{\partial \boldsymbol{Q}}{\partial t}+\frac{\partial \boldsymbol{F}_i}{\partial \xi_i}=\frac{1}{Re}\frac{\partial \boldsymbol{F}_i^v}{\partial \xi_i}+J\boldsymbol{S} \tag{1}$$

with state vector $\boldsymbol{Q}$, convective $\boldsymbol{F}$ and viscous $\boldsymbol{F}_i^v$ flux vectors, and source term $\boldsymbol{S}$. For the Navier–Stokes equations

$$\boldsymbol{Q}=[\rho,\ \rho v_1,\ \rho v_2,\ \rho v_3,\ \rho e]^T \tag{2}$$

$$\boldsymbol{F}_i=\begin{bmatrix}\rho V_i\\ \rho v_1 V_i+\xi_{i,1}p\\ \rho v_2 V_i+\xi_{i,2}p\\ \rho v_3 V_i+\xi_{i,3}p\\ (\rho e+p)V_i\end{bmatrix} \tag{3}$$

and

$$\boldsymbol{F}_i^v=\begin{bmatrix}0\\ f_{1i}\\ f_{2i}\\ f_{3i}\\ v_j f_{ji}+\kappa^*\xi_{i,j}T_{,j}+\mu^*\xi_{i,j}k_{,j}\end{bmatrix} \tag{4}$$

with

$$f_{ji}=\xi_{i,k}\tau_{jk} \tag{5}$$

$$\kappa^*=\kappa[1+(Pr/Pr_T)(\mu_T/\mu)] \tag{6}$$

$$\mu^*=\mu[1+(1/\sigma_k)(\mu_T/\mu)] \tag{7}$$

where τ_{jk}, $j,k:=x,y,z$, are shear and normal stresses. $T_{,j}$ and $k_{,j}$ are partial derivatives of temperature and turbulence kinetic energy in the j direction, μ and μ_T are laminar and eddy viscosity, and σ_k is a turbulence model constant. Because cold gas flows were considered, the laminar viscosity was obtained from Sutherlands law and the static pressure was computed from the perfect gas relation. The thermal conductivity was computed from

$$\kappa=[1/(\gamma-1)PrM^2]\mu \tag{8}$$

The source term

$$\boldsymbol{S}=(1/r)\left[0,0,0,\ p-(1/Re)(\mu+\mu_T)(v_3/r)+\tfrac{2}{3}\rho k,0\right]^T \tag{9}$$

is dependent on the local distance from the axis r and was derived assuming axial symmetry and thin-layer viscous terms in circumferential direction. It replaces the convective and viscous flux differences in circumferential direction.[16] The contravariant velocity V_i is

$$V_i=\xi_{i,j}v_j \tag{10}$$

The nozzle flows that were investigated have regions were the flow is strongly turbulent. For Reynolds-averaged Navier–Stokes (RANS) simulations, the standard two-equation k–ω model of Wilcox[17] was used. The turbulence model state vector, convective and viscous fluxes, and the source term are

$$\boldsymbol{Q}_T=[\rho k,\ \rho\omega]^T \tag{11}$$

$$\boldsymbol{F}_{iT}=\begin{bmatrix}\rho V_i k\\ \rho V_i\omega\end{bmatrix} \tag{12}$$

$$\boldsymbol{F}_{iT}^v=(\mu+\sigma\mu_T)\begin{bmatrix}\xi_{i,j}k_{,j}\\ \xi_{i,j}\omega_{,j}\end{bmatrix} \tag{13}$$

$$\boldsymbol{S}_T=\begin{bmatrix}P_k-Re\beta^*\rho k\omega\\ \alpha\dfrac{\rho}{\mu_T}P_k-Re\beta\rho\omega^2\end{bmatrix} \tag{14}$$

The k-production term is based on the Boussinesq approximation for the Reynolds stresses

$$P_k=(1/Re)\tau_{ij}v_{i,j} \tag{15}$$

The eddy viscosity was computed from

$$\mu_T=\alpha^*(\rho k/\omega) \tag{16}$$

where α^* is equal to 1 for the original model. To assure positive normal Reynolds stresses, a realizability correction was used.[18] The constant α^* was set to c_μ/c_μ^0 with $c_\mu^0=0.09$ and

$$c_\mu=\text{minimum}\left\{c_\mu^0,\ 1\Big/\left[A_0+(A_s/\omega Re)(S^a+W^a)^{1/a}\right]\right\} \tag{17}$$

where $S=|v_{i,j}+v_{j,i}|$ is the total strain and $W=|v_{i,j}-v_{j,i}|$ is the total vorticity. A_0, A_s, and a are model constants. Moore and Moore[18] proposed the constants $A_0=2.85$, $A_s=1.77$, and $a=2$. However, the constants can be chosen differently if a number of conditions are satisfied: To ensure realizability, one must choose $A_s\geq\sqrt{3}$. A_0 has to be set to a value that yields $c_\mu\geq 0.09$ in the log-law region of a boundary layer and in regions where S and W approach 0. In the following, whenever the realizability constants were set to different values, it was verified in a separate calculation of a supersonic boundary layer (not shown) that a c_μ of 0.09 was obtained in the log-law region and in the irrotational and zero stress flow region surrounding it and that the skin-friction prediction was correct. Alternatively, Wilcox's compressible dissipation was used to dampen the turbulence production.[19] Here, the model constants are modified

$$\beta_{\text{corr}}=\beta\left[1-\tfrac{6}{5}\alpha_T F(M_T)\right] \tag{18}$$

$$\beta^*_{\text{corr}}=\beta^*[1+\alpha_T F(M_T)] \tag{19}$$

$$F(M_T)=\left(M_T^2-M_{T_0}^2\right)H\left(M_T-M_{T_0}\right) \tag{20}$$

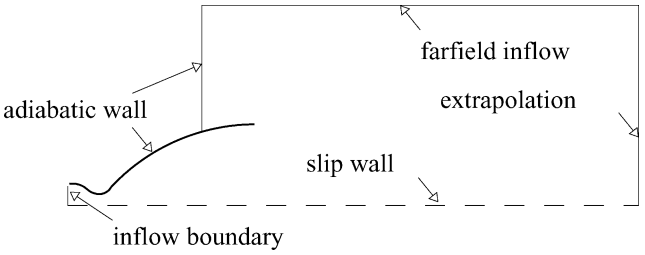

Fig. 4 Boundary conditions.

where $M_T = \sqrt{(2k/c^2)}$ is the turbulence Mach number and $H(\,)$ is the Heaviside function. Without either the realizability correction or the compressible dissipation, the turbulence model overpredicts the Reynolds stresses in the free shear layers of the nozzle flow.

Boundary Conditions

At the nozzle inflow boundary (Fig. 4), all flow quantities were prescribed. Walls were considered to be adiabatic. The velocities at the far-field inflow boundary were extrapolated. Because the velocities were small, the acceleration from the ambient state to the inflow boundary was assumed to be isentropic. The local temperature at the inflow boundary then becomes

$$T = T_a - [(\gamma - 1)M^2/2]\left(v_1^2 + v_2^2\right) \tag{21}$$

The local static pressure is

$$p = p_a(T/T_a)^{\gamma/(\gamma-1)} \tag{22}$$

At the outflow boundary, all flow variables were extrapolated. The centerline was treated as a slip wall.

The turbulence level and the boundary-layer thickness and shape at the inflow boundary were unknowns. Their influence on the separation point has yet to be investigated. For the calculations presented in this paper, the inflow was assumed to be fully laminar, that is, $k \to 0$ and $\mu_T \to 0$, and had constant velocity along the inflow boundary. The dissipation ω at the wall was set to a certain finite value defined by the surface roughness.[19] Because the walls were assumed to be hydraulically smooth, the surface roughness was set to a very small value. Neither turbulence wall functions nor wall distances were needed.

Solver

The EADS-ST finite volume multiblock structured grid RANS code DAVIS-VOL[20,21] was used to obtain solutions of the preceding equations. It features an implicit Euler method for the time integration. Different spatial discretization schemes were employed for the different nozzle simulations,[22–27] (Table 1). The viscous fluxes were discretized by second-order accurate central differences. The steady-state solution is approached iteratively by means of a Newton iteration. To this end, the system of equations is linearized with respect to the primitive variables. The linearized equations are discretized by a first-order upwind scheme for the convective terms and central differences for the viscous terms. The resulting system is solved by a line Gauss–Seidel method. Because only steady-state solutions are sought, the code is not time accurate. An evaluation of the applicability of the numerical approach can be found in Groß and Weiland.[28,29]

However, because of the different strong instability mechanisms involved, for example, shear layer instabilities, the steady-state solution approach only works for separated nozzle flows if the combined diffusion of eddy viscosity and numerical diffusion is strong enough to stabilize the solution.

Nozzle Flow Results

The DLR TIC and the Tehora base nozzle were designed by the method of characteristics (MOC) to give uniform parallel flow in a confined region close to the axis. The absence of the internal shock wave may be responsible for the absence of RSS and the cap shock pattern in ideal nozzles.[5]

Table 1 Discretization schemes

Nozzle	Scheme
	Navier–Stokes convective fluxes
TIC	Second-order accurate Roe-scheme (see Ref. 22)
Tehora	Second-order accurate MAPS$^+$ scheme[23]
All other	Second-order accurate upwind TVD scheme, Yee[24] and Yee and Harten[25]
	Turbulence convective fluxes
TIC (coarse grid)	First-order upwind scheme[26]
All other	Second-order accurate scheme[27]

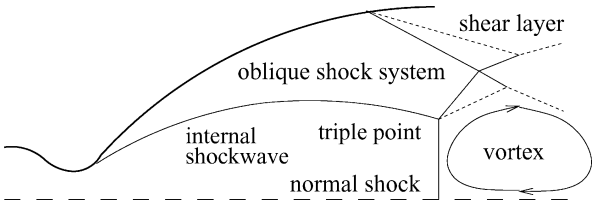

Fig. 5 Schematic of cap shock pattern in parabolic nozzle.

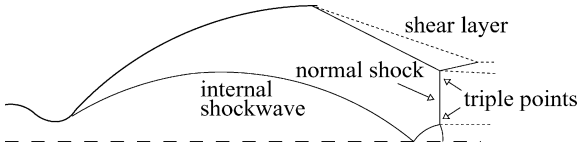

Fig. 6 Schematic of Mach disk in parabolic nozzle.

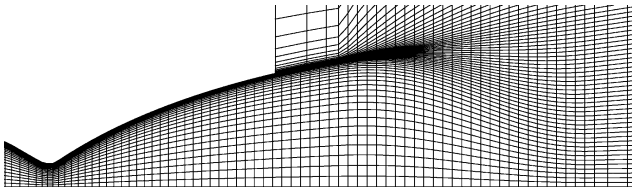

Fig. 7 DLR PAR contour; closeup of computational grid at one-quarter resolution.

Three of the six nozzles studied (DLR PAR, VAC S1, and EADS-ST PARCP) have a thrust-optimized parabolic section and feature an internal shock wave emanating from the nozzle throat. This shock is slightly bent and eventually converges toward the nozzle axis where it gets reflected (Figs. 2, 5, and 6). The DLR PAR contour was designed with the internal shock wave at the same relative location as in the Vulcain nozzle. Because Vulcain shows RSS,[6] RSS was also expected with the DLR PAR contour.

In addition to the RSS shock pattern shown in Fig. 2, parabolic nozzles also show flow separation without reattachment. However, the presence of the internal shock wave results in a shock pattern different from that shown in Fig. 1. The shock pattern features a triple point, as shown in Fig. 5, and is referred to as cap shock pattern.[30] If the strong normal shock is downstream of the reflection point of the internal shock, the deflection of the normal shock by the reflected internal shock is barely visible (Fig. 6). This shock pattern resembles the classical Mach reflection shown in Fig. 1.

The computational grids used for the numerical simulations were body fitted and consisted of two blocks (Fig. 7). The grid resolutions are listed in Table 2. All nozzles were computed on grids with different resolutions. When the change in the solution between subsequent stages of grid refinement was considered to be negligible, the lower, but still sufficient, grid resolution was kept. For the turbulence model used in the current simulations, the laminar sublayer needed to be resolved. This was achieved by keeping the nondimensional wall distance (in wall units y^+) of the wall next cell below 1.

Table 2 Grid resolution

Nozzle	Inside nozzle	Total
TIC	100 × 70	10,800
	200 × 140 (medium)	43,200
	400 × 280 (fine)	172,800
PAR	180 × 152	43,760
VAC S1	200 × 160	49,200
	100 × 80 (coarse)	12,300
Tehora	188 × 100	33,060
TICCP	100 × 50	12,508
PARCP	200 × 100	50,032

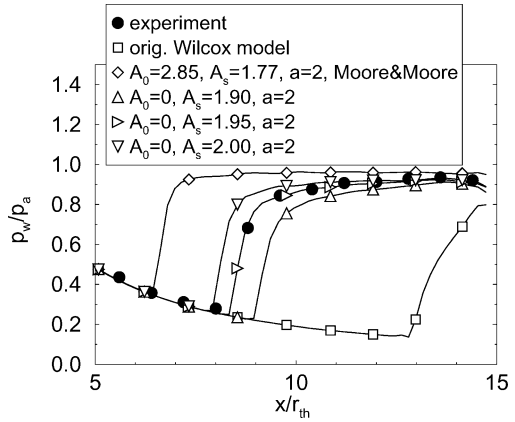

Fig. 8 DLR TIC contour; wall pressure for Wilcox model[17] with and without realizability corrections[18] for $p_c/p_a = 30$.

Fig. 9 DLR TIC contour, pseudo-schlieren plots of computational results (from top to bottom) $p_c/p_a = 10$, 20, 30, 40, 50, 65, and 75.

DLR TIC Contour

For the TIC simulation, the realizability constants were set to $A_0 = 0$, $A_s = 1.95$, and $a = 2$ to match the flow separation location observed in the experiments for $p_c/p_a = 30$ (Fig. 8).

Then, while the realizability constants were kept unchanged, a number of different pressure ratios were computed (Fig. 9). As expected only FSS was observed. Nevertheless, a weak internal shock can still be detected. It may have been caused by a slight difference in the boundary-layer thickness in the simulations compared

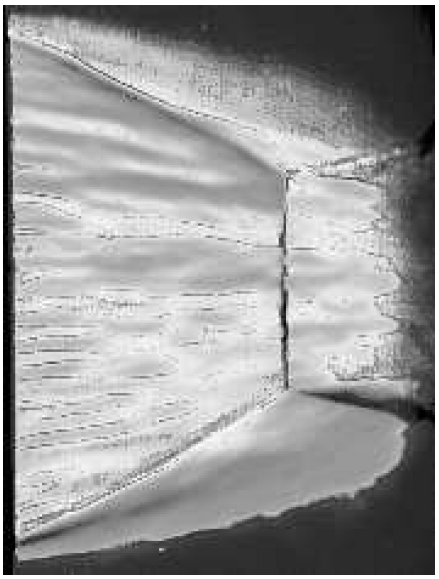

Fig. 10 DLR TIC contour, schlieren image from experiment at DLR.

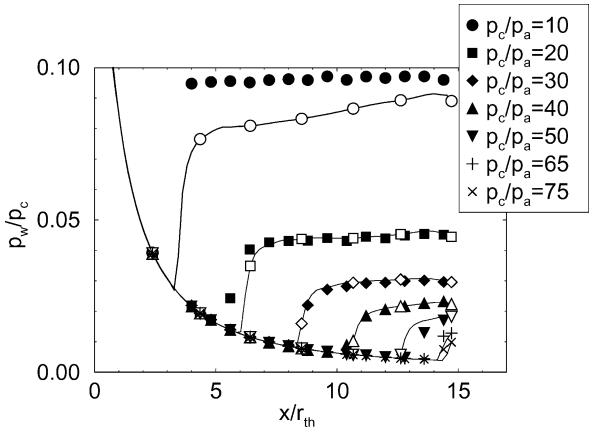

Fig. 11 DLR TIC contour, wall pressure: filled symbols, measurements and open symbols, computations.

to that in the MOC design tool. Thus, in the simulations, the inviscid flow sensed a different geometry than in the MOC design tool resulting in the weak internal shock. This weak shock was reflected at the centerline slightly downstream of the throat but still warped the normal shock for $p_c/p_a \leq 20$. The resulting shock patterns were cap shock for $p_c/p_a \leq 20$ and Mach disk otherwise. The ambient gas was sucked into the nozzle and separated from the nozzle lip, enclosing a small separation bubble. For $p_c/p_a = 65$, the numerical pseudo-schlieren plot compares well with the Schlieren image taken during the test campaign at DLR (Fig. 10). One exception was a weak modulation of the flow in the circumferential direction present in the experiment that was not captured in the axisymmetric simulations. One may speculate that this modulation resulted from a Görtler instability of the boundary layer on the curved nozzle wall.

A comparison of the computed wall pressure with experimental data is given in Fig. 11. When the adapted realizability constants were used, sufficiently accurate separation point predictions could be made for all investigated pressure ratios.

The widely used Schmucker formula[1] provides an empirical relation between the minimum wall pressure, p_i/p_a, upstream of the separation point and the pressure ratio, p_c/p_a. Because the wall pressure, p_w/p_c, is inversely proportional to the downstream coordinate x, it will eventually drop below p_i/p_a. The point where p_i/p_c equals p_w/p_c is the separation location predicted by the Schmucker formula. In Fig. 12, the minimum wall pressure upstream of the

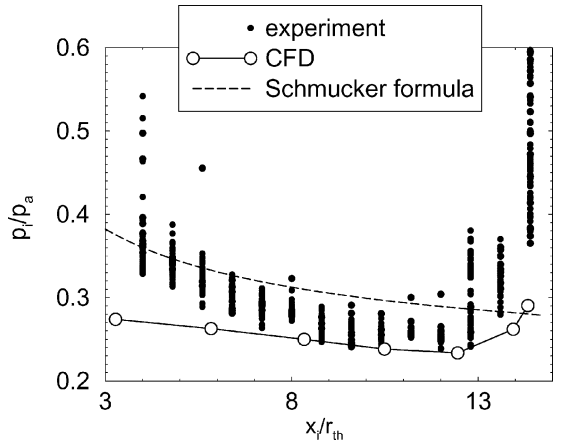

Fig. 12 DLR TIC contour; location of minimum wall pressure.

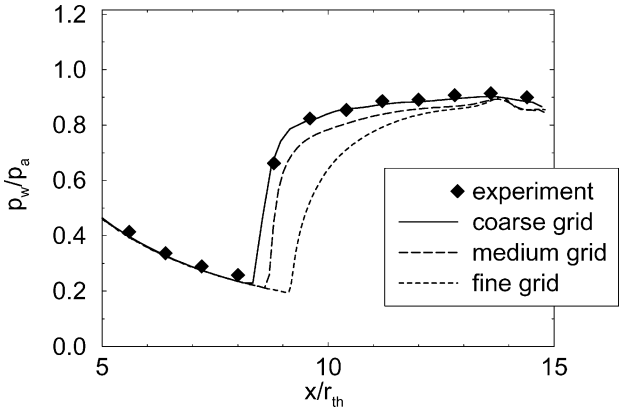

Fig. 13 Grid convergence study for DLR TIC contour for wall pressure, first-order accurate upwind scheme for the turbulence convective fluxes and Roe scheme for the mean flow convective fluxes.

separation point, p_i/p_a, is plotted against the location where it occurs, x/r_{th}. For the experimental results shown, all available wall pressure data were scanned for the point of minimum wall pressure. (For some pressure ratios, several measurements were available.) Figure 12 shows that the ratio p_i/p_a from the simulations was below the experimental results, which means that, for a certain fixed pressure ratio in the simulations, the flow separated from the wall at a lower wall pressure than in the experiment. Therefore, the separation location in the simulation was slightly downstream of the experiment. However, the Schmucker formula is too conservative, predicting the separation location too far upstream. As the separation line approaches the nozzle exit, p_i/p_a increases.[31] This trend, the so called end effect, was captured by the simulations but not by the Schmucker formula.[1]

To prove grid convergence, the $p_c/p_a = 30$ case was computed on a grid with double (medium grid) and quadruple (fine grid) resolution in both directions. Grid convergence could not be achieved (Fig. 13). However, if the Navier–Stokes convective fluxes were discretized with the more accurate upwind total variation diminishing (TVD) scheme[24,25] and the turbulence convective fluxes were discretized with a second-order accurate scheme,[27] grid convergence could be obtained (Fig. 14). The realizability constants then had to be readjusted to match the separation point (Fig. 15). The more accurate discretization was maintained for the following simulations except for the Tehora simulation where the Mach number based advection pressure splitting (MAPS) (Ref. 23) scheme was used for the mean flow convective fluxes.

The dimensionless velocity profiles upstream of the separation point were similar and all matched the logarithmic law (Fig. 16) verifying that the laminar sublayer was well resolved.

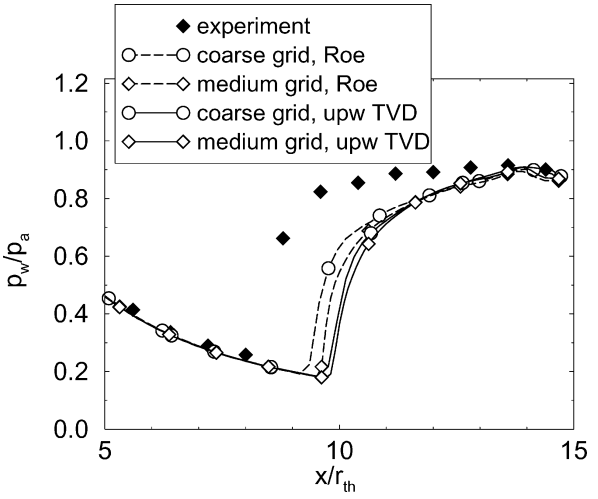

Fig. 14 DLR TIC contour, second-order accurate scheme for the turbulence convective fluxes and Roe and upwind TVD schemes for the mean flow convective fluxes.

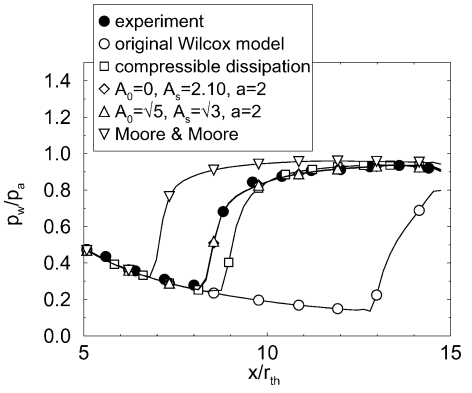

Fig. 15 DLR TIC contour; coarse grid results; wall pressure for original Wilcox model (Ref. 17) and for Wilcox model with Wilcox compressible dissipation (Ref. 19) or realizability corrections (Ref. 18).

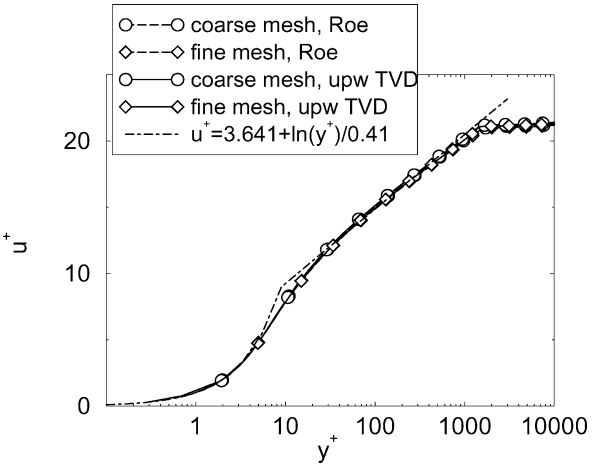

Fig. 16 DLR TIC contour, velocity profiles in wall units upstream of separation at $x = 0.178$ m.

DLR PAR Contour

When the DLR PAR contour was tested at DLR (Fig. 17), RSS was observed during startup in the range $30 \leq p_c/p_a \leq 36$ and during shutdown in the range $36 \geq p_c/p_a \geq 15$. For the numerical simulations, the realizability constants were set to $A_0 = \sqrt{5}$, $A_s = \sqrt{3}$, and $a = 2$. None of the simulation results showed RSS (Fig. 18). Because of the intense internal shock wave, the cap shock pattern is present at all pressure ratios. The flow momentum balance inside the nozzle determines whether RSS or FSS occurs.[3]

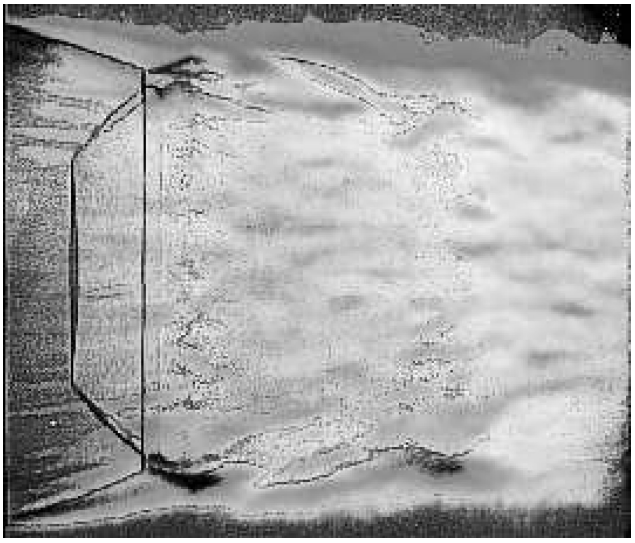

Fig. 17 DLR PAR contour; schlieren image from experiment at DLR.

Fig. 18 DLR PAR contour, pseudo-schlieren plots of computational results (from top to bottom) p_c/p_a = 16, 32, 40, 56, and 72.

A narrow range for RSS indicates a flow momentum balance that is heavily biased toward FSS. Small shortcomings in the numerical method are sufficient to yield faulty FSS predictions in the RSS range.

The wall pressure measurements and computational results are in reasonable agreement (Fig. 19). In Fig. 20, the minimum wall pressure upstream of separation is plotted against the location where it was observed. For the experimental data points shown, all available experimental data were scanned for the lowest wall pressure. For $x/r_{\text{th}} \leq 7$, the simulation's separation pressure is too low when compared with the experimental data. For low-pressure ratios, p_c/p_a, the flow stayed attached to the nozzle wall for too long in the simulations. The experimental data show a branch cut at $x/r_{\text{th}} \approx 8$. This branch cut signals the FSS↔RSS hysteresis region. However, the branch cut is not very pronounced, and the region (and, hence, the pressure ratio range) where it occurred is very narrow.

VAC S1 Contour

The VAC S1 parabolic contour showed RSS in the experiments at FFA.[7] Flow simulation results (same realizability constants as for DLR PAR) are shown in Fig. 21. For $p_c/p_a = 10$,

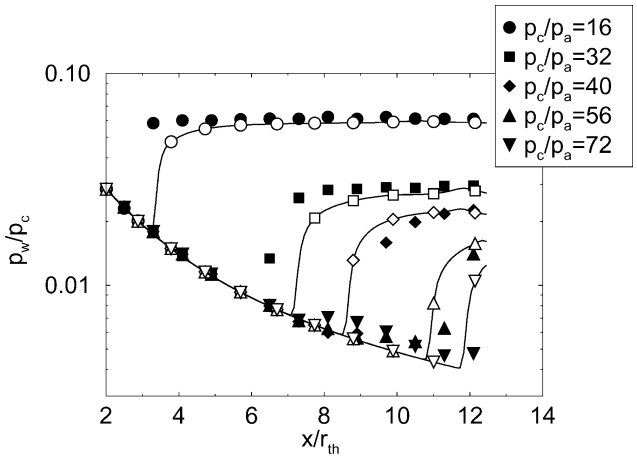

Fig. 19 DLR PAR contour, wall pressure: filled symbols, measurements and open symbols, computations.

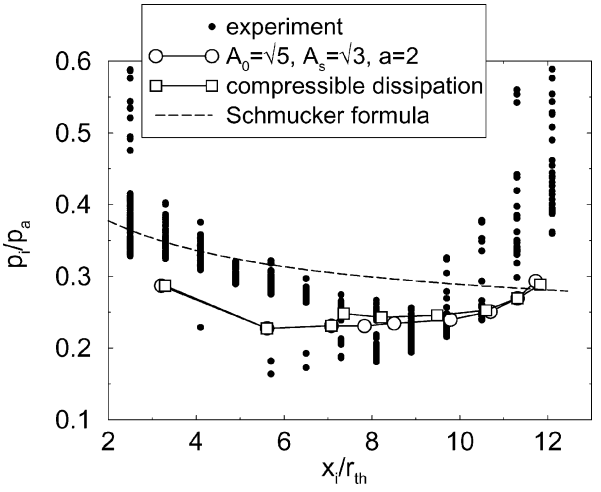

Fig. 20 DLR PAR contour, location of minimum wall pressure.

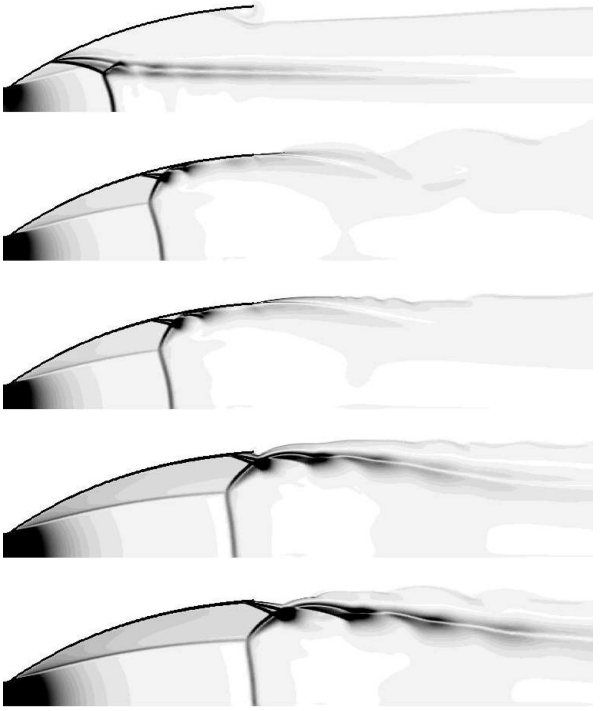

Fig. 21 VAC S1 contour, pseudo-schlieren plots of computational results (from top to bottom) p_c/p_a = 10, 15, 16.5, 29, and 35.

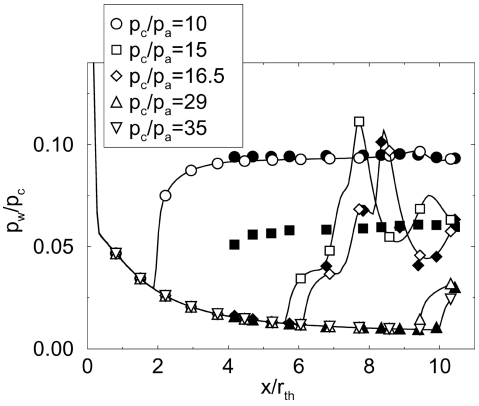

Fig. 22 VAC S1 contour, wall pressure: filled symbols, measurements and open symbols, computations.

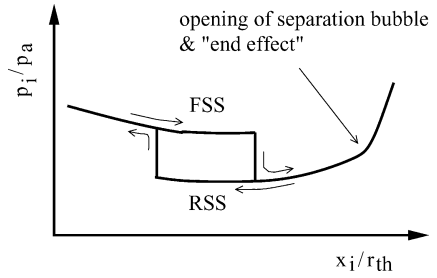

Fig. 23 Schematic of separation location and pressure.

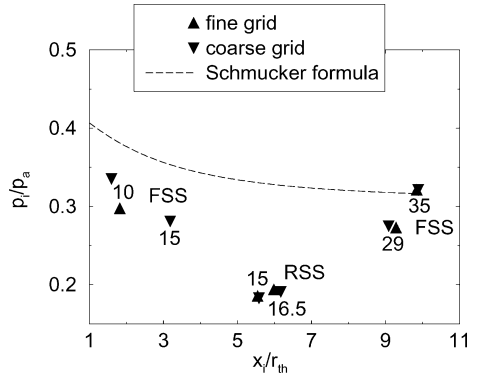

Fig. 24 VAC S1 contour, location of minimum wall pressure from computations for indicated pressure ratios p_c/p_a. Note that for $p_c/p_a = 15$ both an FSS and an RSS solution were obtained on the coarse grid.

29, and 35, FSS was obtained, and for $p_c/p_a = 15$ and 16.5, RSS was obtained. A comparison of the wall pressure distributions is shown in Fig. 22. Whereas the simulation obtained RSS at $p_c/p_a = 15$, FSS was noticed in the experiment for the same pressure ratio.

For nozzles that show a switch from FSS to RSS and back to FSS, a hysteresis has been observed in the experiments (Fig. 23).[7,30] Depending on the flow's history, the pressure ratio at which the switch from RSS to FSS occurs at startup is not the same as that for FSS to RSS during shutdown. During startup, RSS is maintained until the separation bubble opens when it reaches the nozzle exit. Because the static pressure in the separation bubble is below ambient pressure, the separation point is significantly farther downstream in case of RSS than it would be if FSS existed at the same pressure ratio (Fig. 24).

The hysteresis effect appeared in the simulations when the coarse grid was used. Depending on the transient direction, either an RSS or FSS solution could be obtained for $p_c/p_a = 15$ (Fig. 25). However, the RSS solution, after being interpolated onto the fine grid and converged out again, reverted to the FSS solution. When the fine

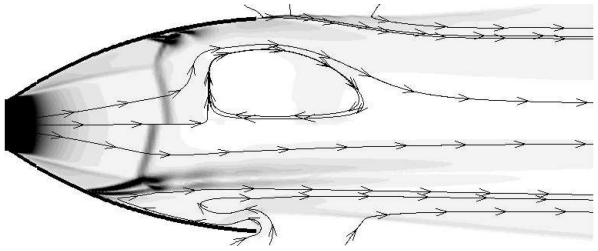

Fig. 25 VAC S1 contour, $p_c/p_a = 15$, coarse grid, pseudo-schlieren plot: RSS (top) or FSS (bottom) depending on flow history.

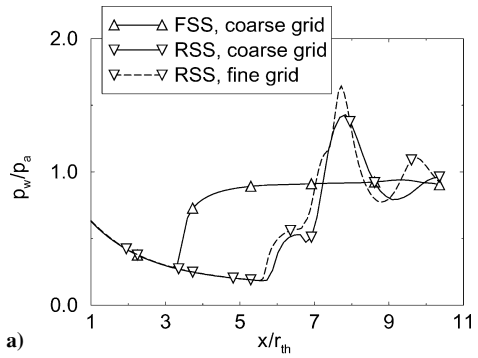

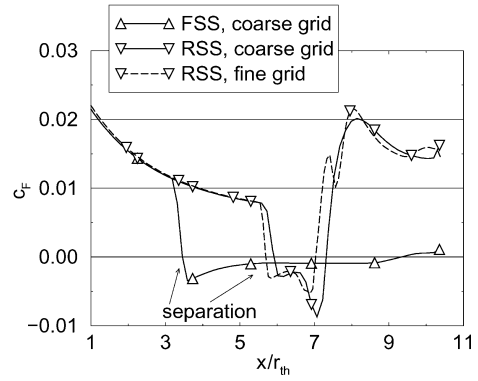

Fig. 26 VAC S1 contour, $p_c/p_a = 15$: a) wall pressure and b) skin-friction coefficient.

grid was used, a hysteresis region could not be observed in the simulations for the pressure ratios chosen.

Comparisons of the FSS and RSS solutions for $p_c/p_a = 15$ are shown in Figs. 26 and 27. For FSS, the wall pressure downstream of the separation point shot up to $\approx 0.9 p_a$. For RSS, it reached a saddle point in the separation bubble of $\approx 0.5 p_a$. Because of the lower pressure, the separation location was much farther downstream for RSS ($x/r_{th} \approx 6$) than for FSS ($x/r_{th} \approx 3.5$). In case of RSS, the reattached supersonic jet went through a series of compression and rarefaction regions, which caused a modulation of the wall pressure downstream of the reattachment point. The strong normal shock crossed the centerline farther upstream in the case of FSS than in the case of RSS (Fig. 25). For RSS, a strong vortex ring was located downstream of the normal shock. On the centerline, reverse flow Mach numbers reached a maximum of ≈ 0.5. This reverse flow formed a stagnation point with the main flow at $x/r_{th} \approx 9$. A second stagnation point was located at $x/r_{th} \approx 17$, which marked the end of the recirculation region. The two stagnation points appear as local pressure maxima on the centerline in Fig. 27. The static pressure at the first stagnation point was $\approx 0.85 p_a$.

Hysteresis effects are well known for steady shock reflections.[32–34] One of the two possible flow patterns is always more stable. If the less stable flow pattern is slightly disturbed, it switches to the other flow pattern, which results in an abrupt change of wall pressure profiles. Figure 26, $p_c/p_a = 15$, provides an example of

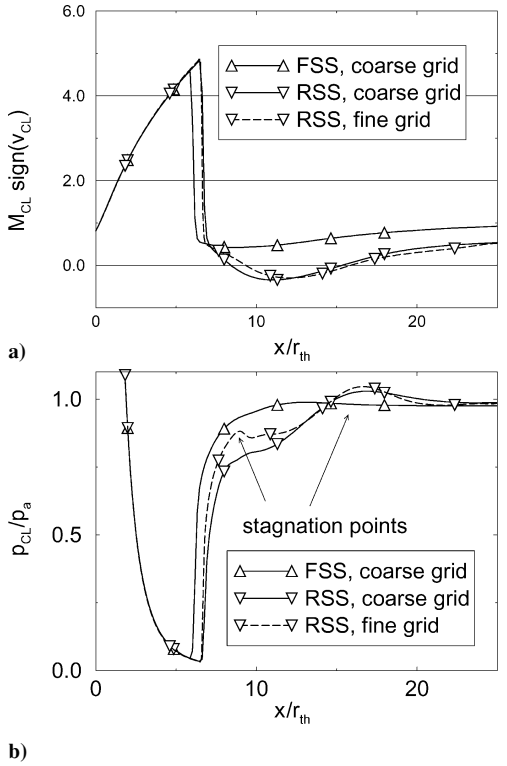

Fig. 27 VAC S1 contour, $p_c/p_a = 15$: a) centerline Mach number and b) pressure.

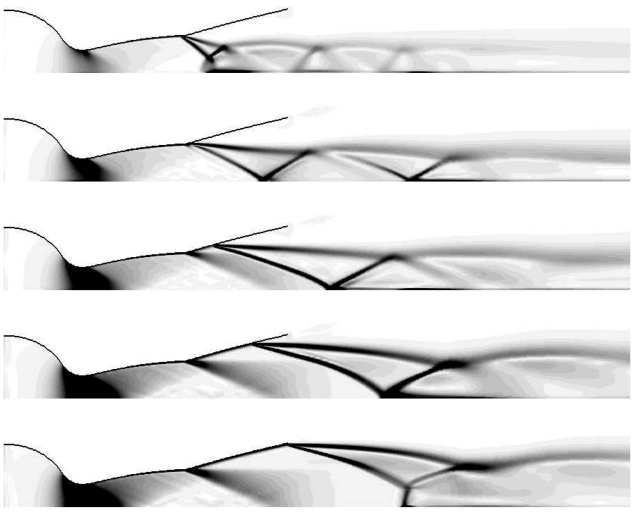

Fig. 28 EADS-ST Tehora dual bell contour, pseudo-schlieren plots of computational results (from top to bottom) $p_c/p_a = 6$, 12, 18, 24, and 40.

the difference in wall pressure profiles for two flow patterns. During the rocket engine startup, the separation point and the normal shock move downstream toward the nozzle exit. The duration of this transient depends mainly on the startup characteristics of the turbopumps and takes about 3 s for large cryogenic engines. As proposed by several authors,[3–6] the sudden switch from FSS to RSS and RSS to FSS during this transient may be a major contributor to side loads.

Tehora Dual Bell Contour

For the Tehora simulation, the compressible dissipation by Wilcox (Ref. 19) was used instead of the realizability correction (Ref. 18). Pseudo-schlieren plots are shown in Fig. 28. At pressure ratios where the flow separated at the contour discontinuity, there was no obvious strong shock in vicinity of the centerline. Although regular shock reflections at the centerline do not exist in axisymmetric flows, the oblique shock appeared to be reflected at the nozzle axis. (If the grid and image resolution were better, a miniature normal shock would be visible at the centerline.[35]) Downstream of the first oblique shock, the flow was still supersonic. Consequently, a second oblique shock had to form. The resulting succession of oblique shocks and expansion regions resembles the diamond-shaped pattern found in underexpanded supersonic jets. The wall pressure distributions are shown in Fig. 29. Because the pressure gradient in the extension nozzle was steep, the separation point shifted downstream slowly as the pressure ratio was increased. A binary switch between the two operating modes (separation at the contour discontinuity or at the nozzle exit) would be more desirable because sudden changes are believed to be more predictable and, hence, easier to control.

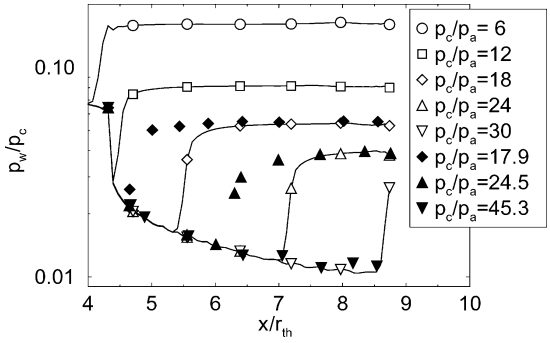

Fig. 29 EADS-ST Tehora dual bell contour, wall pressure: filled symbols, measurements and open symbols, computations.

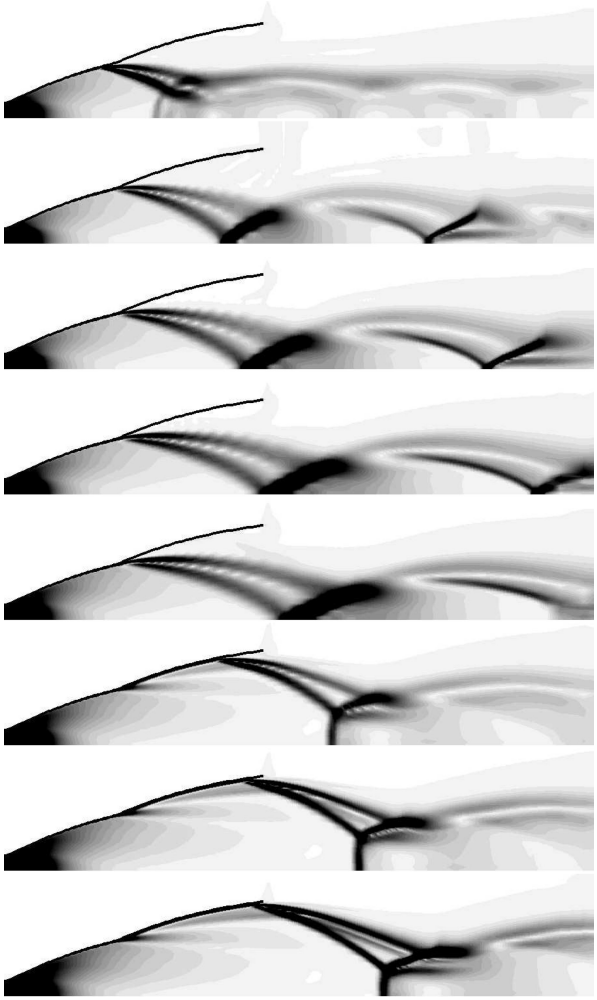

Fig. 30 EADS-ST TICCP contour, pseudo-schlieren plots of computational results (from top to bottom) $p_c/p_a = 30$, 40, 50, 60, 70, 80, 90, and 100.

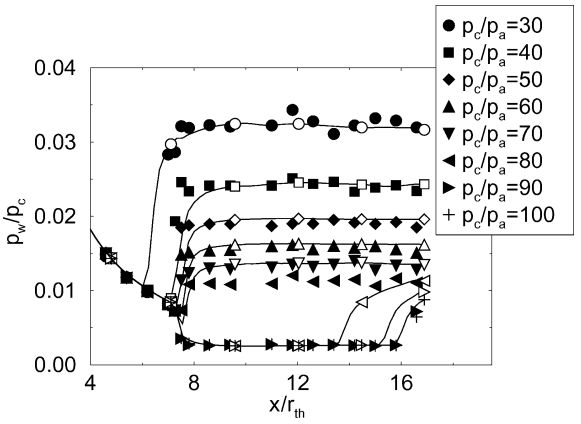

Fig. 31 EADS-ST TICCP contour, wall pressure: filled symbols, measurements and open symbols, computations.

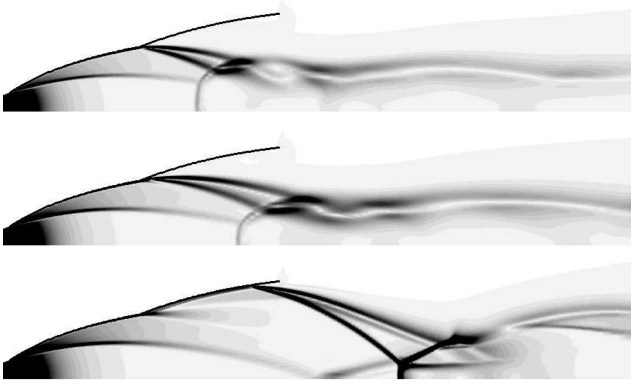

Fig. 32 EADS-ST PARCP contour, pseudo-schlieren plots of computational results (from top to bottom) $p_c/p_a = 50$, 70, and 90.

The base nozzle contour was designed with MOC without further smoothing. Minute wall normal displacements y of the contour lead to pressure fluctuations Δp

$$\Delta p = \frac{\rho v^2}{\sqrt{M^2 - 1}} \frac{\partial y}{\partial s} \tag{23}$$

along the wall arc length s (Ref. 36).

EADS-ST TICCP Contour

The TICCP contour and the following PARCP contour were developed at EADS-ST in the framework of the German national technology program on cryogenic engine research (TEKAN).[8] Both nozzles have constant pressure extensions to allow for a quick change between the two operating modes. For both simulations, the realizability correction with $A_0 = \sqrt{5}$, $A_s = \sqrt{3}$, and $a = 2$ was used. For pressure ratios between 40 and 70, the flow separated at the contour discontinuity (Fig. 30). For larger pressure ratios, the separation rapidly approached the nozzle exit. As before in case of the Tehora contour, the supersonic jet was underexpanded when it separated at the contour discontinuity. This again lead to a sequence of expansion regions and oblique shocks downstream of the initial shock. The simulation results for pressure ratios above 70 show a pronounced Mach disk and another oblique shock wave in the supersonic flow, emanating from the contour discontinuity.

The corresponding wall pressure distributions are given in Fig. 31. For pressure ratios less than 80, the simulation results were very close to the experiment. Above 80, the calculated separation locations were too far upstream. The design goal of an almost binary mode switch was validated in the experiments and was roughly reproduced in the simulations.

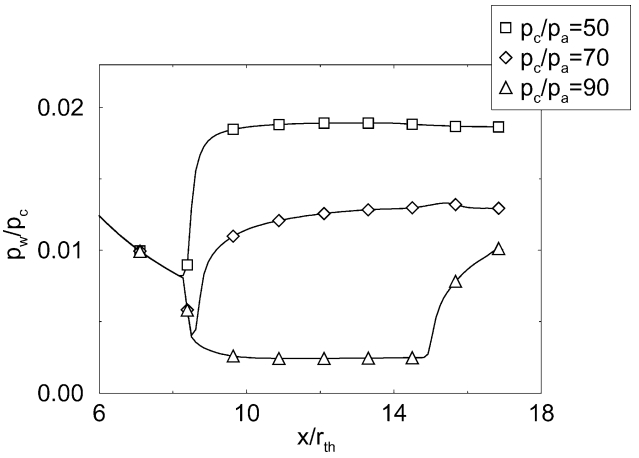

Fig. 33 EADS-ST PARCP contour, wall pressure.

EADS-ST PARCP Contour

The last contour considered herein features a parabolic base nozzle. The simulation results show a pronounced internal shock wave originating at the nozzle throat (Fig. 32). For $p_c/p_a = 50$ and 70, this shock wave interacted with the normal shock, which resulted in the cap shock pattern. At $p_c/p_a = 90$, the normal shock was downstream of the internal shock wave reflection off the axis. As a result, the cap shock pattern disappeared. This nozzle also displayed an oblique shock emanating from the contour discontinuity.

Wall pressure distributions from the simulations are shown in Fig. 33. As with the TICCP contour, the separation point moved rapidly downstream as the pressure ratio rose above 70. Therefore, this nozzle also displays the almost binary operation mode switch.

Conclusions

Numerical simulations of a truncated ideal, two parabolic, and three dual bell nozzles were performed for different pressure ratios. The realizability constants were tuned to obtain reasonable agreement between the simulations and the experiments.

The simulations indicated FSS is the only separation mechanism possible for the DLR TIC contour. This may be attributed to the absence of a pronounced internal shock wave. For the DLR parabolic nozzle, RSS was not found in the simulations. The pressure ratio range for which RSS occurred in the experiments for that nozzle was very narrow. Accurate predictions of the flow momentum balance in the nozzle have to be made to predict RSS correctly. A narrow RSS range is an indication of a delicately balanced flow. Minor inaccuracies of the numerical method can lead to faulty predictions. For both nozzles, an increase of the separation pressure p_i/p_a could be observed as the separation approached the nozzle exit. This confirms the existence of the end effect. For the VAC S1 parabolic nozzle, RSS was calculated. The existence of an FSS↔RSS hysteresis region, where the separation mechanism depends on the flow history, could be simulated on a coarse grid. When a finer grid was used, the hysteresis could not be shown for the pressure ratios chosen. Here the solution obviously depends on the grid resolution. Therefore, although the results obtained from the coarse grid were used to point out differences in wall pressure and separation point locations, and to highlight phenomenological differences of the overall flow, they can not be seen as a proof for the existence of a hysteresis region.

Three dual bell nozzles were computed as test cases for more complex nozzle geometries. Here, characteristic flow phenomena (diamond-shaped pattern of underexpanded supersonic jet, oblique shock emanating from contour discontinuity) were pointed out in a qualitative manner. For the dual bell nozzles with zero pressure gradient extension, the binary operation mode switch was less pronounced in the simulations than in the experiments.

For the results shown in this paper, the realizability constants were modified to match predicted flow separation locations with the experiment. Obviously, the calculated separation point prediction is strongly dependent on the model constants chosen, which

indicates the turbulence models' inability to capture all of the relevant aspects of the turbulence dynamics. If the numerical method described herein was to be used for flow predictions where no experimental data were available, this would be unacceptable. Nevertheless, once the model constants are calibrated, it can be used for careful interpolations between available experimental data or to complement experimental data by providing flow data that can not be measured. The question whether a significant improvement of the predictive capabilities of the numerical method could be made by incorporating more complex turbulence models remains unanswered. To make correct predictions of the shear layer spreading rates, it may be essential that the dynamics of the large turbulent coherent structures are accounted for. After all, nozzle flows are dominated by shear layers, and accurate predictions of, for example, the momentum balance inside the nozzle (which determines the occurrence of either FSS or RSS) are likely very dependent on correct predictions of the shear layer physics. Other assumptions made, for example, the assumption of steady, axisymmetric flow, must also be questioned. More fundamental research of the different aspects of separated nozzle flows has to be conducted to build confidence in the numerical approach and the turbulence model used.

Acknowledgments

This work was in part supported by the German national technology program on cryogenic engine research (TEKAN) and the European Flow separation control device (FSCD) technology programs. The authors wish to acknowledge the cooperation, helpful discussions, and support received from the various persons involved in both programs.

References

[1]Schmucker, R. H., "Status of Flow Separation Prediction in Liquid Propellant Rocket Nozzles," NASA TM X-64890, Nov. 1974.

[2]Nave, L. H., and Coffey, G. A., "Sea Level Side Loads in High-Area-Ratio Rocket Engines," AIAA Paper 73-1284, Nov. 1973.

[3]Frey, M., and Hagemann, G., "Flow Separation and Side-Loads in Rocket Nozzles," AIAA Paper 99-2815, June 1999.

[4]Frey, M., "Shock Patterns in the Plume of Overexpanded Nozzles," *Proceedings of the 3rd European Symposium on Aerothermodynamics for Space Vehicles*, ESA-European Space Research and Technology Center (ESTEC), ESA SP-426, Noordwijk, The Netherlands, 1999, pp. 395–402.

[5]Frey, M., and Hagemann, G., "Status of Flow Separation Prediction in Rocket Nozzles," AIAA-98-3619, 1998.

[6]Terhardt, M., Hagemann, G., and Frey, M., "Flow Separation and Side-Load Behavior of the Vulcain Engine," AIAA Paper 99-2762, June 1999.

[7]Mattsson, J., Högmann, U., and Torngren, L., "A Subscale Test Program on Investigation of Flow Separation and Sideloads in Rocket Nozzles," *Proceedings of the 3rd European Symposium on Aerothermodynamics of Space Vehicles*, ESA–European Space Research and Technology Centre (ESTEC), ESA SP-426, Noordwijk, The Netherlands, 1998, pp. 373–378.

[8]Hagemann, G., Terhardt, M., Haeseler, D., and Frey, M., "Experimental and Analytical Design Verification of the Dual-Bell Concept," *Journal of Propulsion and Power*, Vol. 18, No. 1, 2002, pp. 116–122; also AIAA Paper 2000-3778, July 2000.

[9]Kusaka, K., Kumakawa, A., Niino, M., Konno, A., and Atsumi, M., "Experimental Study on Extendible and Dual-Bell Nozzles under High Altitude Conditions," AIAA Paper 2000-3303, July 2000.

[10]Haidinger, F. A., Görgen, J., and Haeseler, D., "Numerical Prediction of Flow Separation for Advanced Nozzle Concepts," AIAA Paper 98-3368, July 1998.

[11]Frey, M., Stark, R., Ciezki, H. K., Quessard, F., and Kwan, W., "Subscale Nozzle Testing at the P6.2 Test Stand," AIAA Paper 2000-3777, July 2000.

[12]Chen, C. L., Chakravarthy, S. R., and Hung, C. M., "Numerical Investigation of Separated Nozzle Flows," *AIAA Journal*, Vol. 32, No. 9, 1994, pp. 1836–1843.

[13]Nasuti, F., and Onofri, M., "Viscous and Inviscid Vortex Generation During Nozzle Flow Transients," AIAA Paper 96-0076, Jan. 1996.

[14]Hunter, C. A., "Experimental, Theoretical, and Computational Investigation of Separated Nozzle Flows," AIAA Paper 98-3107, July 1998.

[15]Schröder, W., and Behr, R., "WP2: Numerical Simulation (3D) of Flow Separation and Side Load Prediction," Internal Report, EADS-ST, 81663 Munich, Germany, Sept. 1994.

[16]Nietubicz, C. J., Pulliam, T. H., and Steger, J. L., "Numerical Solution of the Azimuthal-Invariant Thin-Layer Navier–Stokes Equations," *AIAA Journal*, Vol. 18, No. 12, 1980, pp. 1411, 1412.

[17]Wilcox, D. C., "Reassessment of the Scale-Determining Equation for Advanced Turbulence Models," *AIAA Journal*, Vol. 26, No. 11, 1988, pp. 1299–1310.

[18]Moore, J. G., and Moore, J., "Realizability in Two-Equation Turbulence Models," AIAA Paper 99-3779, June–July 1999.

[19]Wilcox, D. C., "Progress in Hypersonic Turbulence Modeling," AIAA Paper 91-1785, June 1991.

[20]Schröder, W., and Hartmann, G., "Computation of 3D Viscous Hypersonic Flows," *Proceedings of the 4th International Symposium on Computational Fluid Dynamics*, Univ. of California, Davis, CA, Sept. 1991.

[21]Schröder, W., and Hartmann, G., "Implicit Solutions of Three-Dimensional Viscous Hypersonic Flows," *Computer and Fluids*, Vol. 21, No. 1, 1992, pp. 109–132.

[22]Chakravarthy, S. R., "High Resolution Upwind Formulations for the Navier–Stokes Equations," von Karman Inst. for Fluid Dynamics, VKI LS 1988-05, Rhode-Saint-Genèse, Belgium.

[23]Rossow, C.-C., "A Flux Splitting Scheme for Compressible and Incompressible Flows," AIAA Paper 99-3346, Jan. 1999.

[24]Yee, H. C., "Upwind and Symmetric Shock-Capturing Schemes," NASA TM 89464, May 1987.

[25]Yee, H. C., and Harten, A., "Implicit TVD Schemes for Hyperbolic Conservation Laws in Curvilinear Coordinates," *AIAA Journal*, Vol. 25, No. 2, 1987, pp. 266–274.

[26]Weber, C., Behr, R., and Weiland, C., "Investigation of Hypersonic Turbulent Flow over the X-38 Crew Return Vehicle," AIAA Paper 2000-2601, June 2000.

[27]Schröder, W., and Mergler, F., "Investigation of the Flowfield over Parallel-Arranged Launch Vehicles," AIAA Paper 93-3060, July 1993.

[28]Groß, A., and Weiland, C., "Investigation of Shock Patterns and Separation Behavior of Several Subscale Nozzles," AIAA Paper 2000-3293, July 2000.

[29]Groß, A., "Numerische Untersuchung abgelöster Düsenströmungen," Ph.D. Dissertation, Rheinisch-Westfälische Technische Hochschule Aachen, Aachen, Germany, 2002.

[30]Hagemann, G., Frey, M., and Koschel, W., "Appearance of Restricted Shock Separation in Rocket Nozzles," *Journal of Propulsion and Power*, Vol. 18, No. 3, 2002, pp. 577–584.

[31]Sunley, H. L. G., and Ferriman, V. N., "Jet Separation in Conical Nozzles," *Journal of the Royal Aeronautical Society*, Vol. 68, No. 648, 1964, pp. 808–817.

[32]Vuillon, J., Zeitoun, D., and Ben-Dor, G., "Numerical Investigation of Shock Wave Reflections in Steady Flows," *AIAA Journal*, Vol. 34, No. 6, 1996, pp. 1167–1173.

[33]Chpoun, A., Passerel, D., and Ben-Dor, G., "Stability of Regular and Mach Reflection Wave Configurations in Steady Flows," *AIAA Journal*, Vol. 34, No. 10, 1996, pp. 2196–2198.

[34]Ivanov, M. S., Gimelshein, S. F., and Beylich, A. E., "Hysteresis Effect in Stationary Reflection of Shock Waves," *Physics of Fluids*, Vol. 7, No. 4, 1995, pp. 685–687.

[35]Mölder, S., Gulamhussein, A., Timofeev, E., and Voinovich, P., "Focussing of Conical Shocks at the Centre-Line of Symmetry," *Proceedings of the 21st International Symposium on Shock Tubes and Shock Waves*, University of Queensland, Dept. of Mechanical Engineering, St. Lucia, Queensland, 1998.

[36]Liepmann, H. W., and Roshko, A., *Elements of Gasdynamics*, Addison Wesley, Reading, MA, 1957.